POLITECNICO DI TORINO
Repository ISTITUZIONALE

Direct Fabrication of Ultrahydrophobic Laser-Induced Graphene for Strain Sensors

(Article begins on next page)

02 September 2025

Article

Direct Fabrication of Ultrahydrophobic Laser-Induced Graphene for Strain Sensors

Devanarayanan Meena Narayana Menon [ID], Matteo Giardino [ID] and Davide Janner *[ID]

Department of Applied Science and Technology (DISAT) and RU INSTM, Politecnico di Torino, Corso Duca degli Abruzzi 24, 10129 Torino, Italy
* Correspondence: davide.janner@polito.it

Abstract: Laser-induced graphene (LIG) has garnered tremendous attention in the past decade as a flexible, scalable, and patternable alternative for fabricating electronic sensors. Superhydrophobic and superhydrophilic variants of LIG have been demonstrated by previous studies. However, stability analysis of the superhydrophobic surface property has not been explored. In this study, we use an infrared nanosecond laser to fabricate reduced graphene oxide (rGO)-based strain sensor on a carbon fiber reinforced polymer (CFRP) composite substrate. The fabricated sensor is characterized to determine its gauge factor using a three-point bend test demonstrating a gauge factor of 40. The fabricated LIG exhibits excellent superhydrophobic properties with a high contact angle (>160°). Both superhydrophobicity and piezoresistivity of the LIG under water immersion are studied for 25 h, demonstrating high stability. The obtained results could be of interest to several sectors, especially for maritime and high humidity applications.

Keywords: superhydrophobic; laser-induced graphene; strain sensors; carbon fiber composites; nanosecond laser

1. Introduction

Fiber-reinforced polymer composites are progressively replacing conventional materials such as metals, alloys, and ceramics in aerospace, infrastructure, and maritime industries [1–3]. This is due to their mechanical properties, such as superior strength, high elastic modulus, thermal insulation, lightweight footprint, and corrosion resistance [4–6]. However, due to their complex structure, composite materials are prone to various structural failures in their matrix phase, reinforcing phase, and debonding [7,8]. Additionally, for composites, failure accumulation occurs over some time. Therefore, performing structural health monitoring of the composite material is crucial to schedule timely maintenance and prevent any catastrophic failure while in application [9].

Commercially available strain gauges are generally based on metallic and semiconductor materials. Although these strain gauges are cost-effective and represent the commercial grade, they suffer from critical limitations such as poor mechanical flexibility, low sensitivity, and inability to function in extreme conditions such as those underwater [10,11] As an alternative, piezoresistive materials such as carbon nanotubes (CNT) and Graphene/Graphene-oxide based materials are currently being investigated to fabricate strain sensors [12–14]. Ming Lei et al. fabricated a waterproof, flexible, and wearable strain sensor using CNT/Carbon-black [15]. In comparison to the chemical-based sensor fabrication approach, laser material processing for surface texturing/chemical modification has attracted tremendous interest recently as a cost-effective approach [16,17]. Rapid fabrication along with the possibility for selective surface patterning with laser represents a more scalable approach [18–20]. In this frame of reference, laser-induced graphene (LIG) from polymer precursors such as polyimide (PI) are being increasingly studied as an alternative means to fabricate strain sensors [21–24].

As strain sensors also involve outdoor applications, the LIG material must be functionally stable under extreme conditions such as high humidity or water immersion [25,26]. Towards this consideration, the natural water repellency of the superhydrophobic surface could prevent the gradual functional degradation of the sensor under humid conditions. Lu Wang et al. fabricated by laser processing a porous graphene surface coated with fluorosilane to obtain a superhydrophobic and efficient anti-icing and de-icing surface [27]. Li et al. directly fabricated a superhydrophobic LIG by performing laser ablation in an argon environment [28]. Although the above-mentioned methods achieve excellent water-repellent properties, the scalability and simplicity in fabrication, at the core of LIG-based sensors and functional surfaces, remains a challenge. In certain applications, such as electrochemical sensing, there is a need for the fabrication of miniaturized electrodes [29]. In such cases, the comparatively large-size features fabricated by CO_2 lasers could be disadvantageous, whereas UV lasers are relatively expensive. In this context, NIR industrial fiber laser systems with high tunability in laser parameters such as pulsewidth, pulse repetition rate, average power, and scan speed offer greater flexibility to the fabrication process. These systems enhance precision surface modification due to their relatively short wavelength, thanks to their tunable low-pulsewidth in the nanosecond regime.

Few researchers have taken advantage of the tunability of laser writing parameters to minimize the surface oxidation of exposed LIG to maintain its hydrophobic property [30–32]. The hydrophobicity provided by the surface carbon content along with the rough and hierarchical surface texture of LIG could result in surface superhydrophobicity. These studies successfully demonstrate a one-step fabrication approach of superhydrophobic LIG. However, in most of these studies, the water contact angle (CA) values are on the lower threshold limit for superhydrophobicity (CA = 150°). Moreover, to our knowledge, no study has characterized the stability of fabricated LIG superhydrophobic surfaces under extreme conditions. Indeed, such characterizations are necessary to ascertain the stability of the superhydrophobic property for applications.

In this work, an LIG-based strain sensor was fabricated on a polyimide tape directly adhered onto a carbon fiber composite (CFRP) material, obtaining a gauge factor (GF) of about 40. Additionally, the laser parameters were selected such that the LIG sensor was rendered superhydrophobic with high CA (~165°). Finally, the stability of superhydrophobicity was demonstrated by continuous immersion underwater for 25 h, droplet impact and water-jet impact. The combined properties of high sensitivity with a highly stable superhydrophobic state could boost the commercial applicational prospects of LIG.

2. Materials and Methods

2.1. LIG Fabrication

An infrared (1064 nm, Nd:YvO4) fiber nanosecond laser system (Datalogic Arex 20 MW, Bologna, Italy) was used to fabricate LIG. The laser system consists of a galvanometric optical scan system coupled with an F-theta lens enabling flexible and easy fabrication of software-designed patterns using the (Lighter MARVIS software). For all the modifications performed in this study, the scan speed and pulse repetition rate were fixed at 3 mm/s and 22 kHz, respectively. For laser fabrication of the sensor, an average power of 9 W was used. A Direct Laser Writing (LDW) approach was used to generate LIG from the polyimide Kapton tape through a thermal decomposition process, as shown in Figure 1. Since the precursor is in the form of a polyimide tape, the laser-generated LIG is independent of the base substrate. To demonstrate the fabrication of LIG on various substrates, soda-lime glass, aluminum alloy (Al 6061), low density polyethylene (LDPE) and silicon were used as the base substrates.
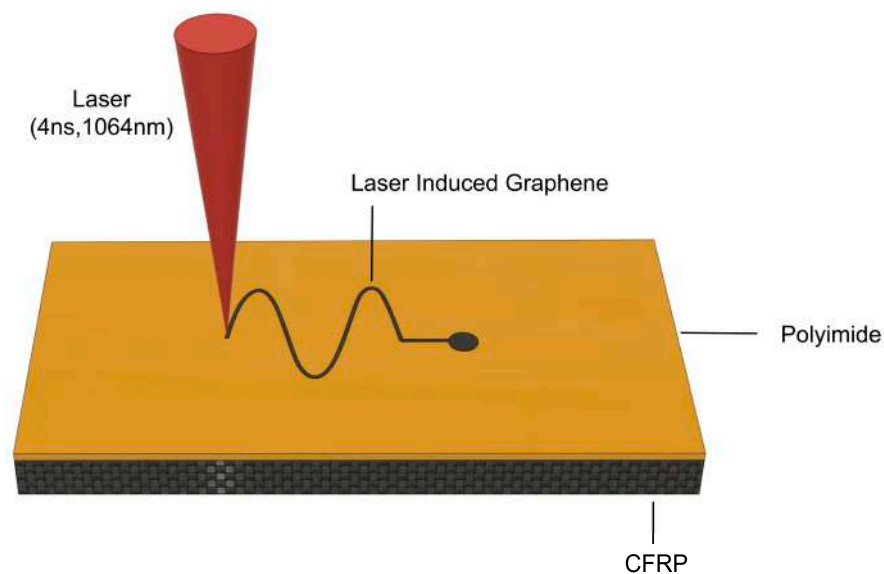
Figure 1. Illustration of the laser fabrication process of LIG on polyimide attached on a carbon fiber reinforced polymer (CFRP) part.

2.2. Surface Morphology and Chemical Composition Analysis

A field emission scanning electron microscope (FESEM, SupraTM 40, Zeiss, Germany), at an accelerating voltage of 2 kV was used to analyze the surface morphology of the generated LIG. The system was also equipped with an energy dispersive X-ray analyzer (EDS, Bruker, Germany). Gold coating was used while taking EDS measurements.

A confocal Raman microscope InVia Renishaw (Renishaw, New Mills, UK) was used to analyze the laser-induced transformation to the graphene-based material. The measurement was obtained in high confocality mode, using a laser excitation wavelength of 532 nm at an average power of 300 uW.

Fourier Transform Infrared Spectroscopy (FTIR) analysis was performed to study the LIG obtained on a flat polished aluminum substrate in reflection mode with a Shimadzu IR Tracer 100 FTIR Spectrophotometer along with a Shimadzu AIM-9000 Infrared microscope.

2.3. Sensor Fabrication and Analysis

LIG circuit was laser generated on top of the carbon fiber reinforced composite material (CFRP, 2.8 mm thick) to fabricate the strain sensor which had an insulating outer layer as received. Fast-drying silver paint (Ted Pella, Redding, CA, USA) was used as the contact points which were connected to copper lead wires for four-probe measurements. Three-point bending tests were performed under flexure to characterize the strain sensing property of the fabricated LIG sensor. The mechanical sensing tests were performed at room temperature (22 ± 1 °C) using a Zwick Roell Z100 machine with a load cell of 5 kN, rate of 0.5 mm min^{-1}, edge-to-edge spacing of 10 mm and maximum deformation of the loading nose at 1 mm. Throughout the bending test, the relative change in resistance was monitored synchronously using the four probe connections to the digital multimeter (Keithley DMM6500, Tektronix, OR, USA).

2.4. Superhydrophobic Surface Characterization

Dynamic contact and sliding angle measurements were used to characterize the surface wettability of the surface. A contact angle measurement system (DSA 100, KRÜSS Scientific, Hamburg, Germany) with an inbuilt goniometer stage was used to perform the measurements.

The droplet bounce on the superhydrophobic surface was taken using the backlight technique with a high-speed camera (Chronos 1.4, Kron technologies, Burnaby, BC, Canada)

at a fixed frame rate of 1059 fps. All the static and dynamic measurements in the experiment were performed with a droplet volume of 6 μL.

3. Results and Discussion

3.1. Surface Material Characterization

Laser-induced graphene (LIG) from polymeric precursors is usually fabricated using a CO_2 or ultraviolet laser [33–36]. The electron microscope images in Figure 2a,b reveal certain interesting surface modification features. Interestingly, beside the laser-modified track, a swollen region is observed. The swell is a result of material expansion occurring at laser fluence below the ablation threshold. Multiple factors could contribute to the swell formation, such as non-equilibrium cooling of the polymer melt and polymer surface expansion due to the pressure effect as a result of gaseous and volatile substance release during the ablation process [37,38]. Furthermore, Figure 2a,b shows random bubbles in the laser modified region. Such a bubble formation can be attributed to a first order phase transition generally observed with laser interaction of relatively transparent polymers.
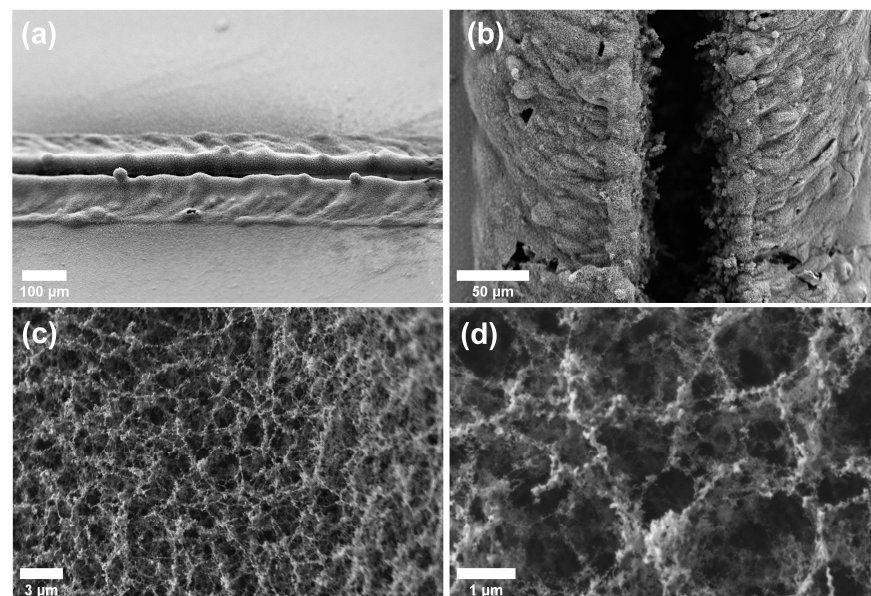

Figure 2. Field Emission Scanning electron microscope images of the fabricated LIG, (**a**,**b**) Side and top view of the ablated and swollen laser-modified region; (**c**,**d**) magnified images of the porous and fibrous LIG network in the central ablated region.

The bulk boiling and the eventual rapid cooling results in the formation of such bubble-like features.

Figure 2c,d shows the electron microscope images of the reduced graphene oxide's porous and fibrous network structure. This agrees with the LIG generation mentioned in previous studies which have confirmed a heptagon-pentagon and hexagon hybrid lattice due to the laser-induced localized temperature and pressure at a short timescale [39,40]. The formation mechanism of the reduced graphene oxide can be attributed to a photothermal pyrolysis process [41,42]. In comparison to the UV and CO_2 laser wavelengths used to generally perform LIG fabrication, the polyimide has a relatively lower absorption cross-section at 1064 nm. Therefore, a multi-pulse incubation effect initiates the thermal degradation of the polyimide to an amorphous carbon form with a better absorption cross-section, eventually leading to ablation of the material and formation of LIG [43,44].

The Raman spectra shown in Figure 3 suggest the formation of reduced graphene oxide. Two higher intensity peaks representing G and D bands, typical to carbonaceous materials, are observed. The G band at 1580 cm^{-1} corresponds to the graphitic lattice stretching of sp^2 carbon atoms. The disorder band (D-band) at 1335 cm^{-1} is attributed to

the breathing vibrations of the sp^2 hybridized carbon [45]. The band mainly arises due to the restriction of carbon vibrations due to oxygen-containing functional groups acting as defects to the material structure. Indeed, an Id/Ig ratio of D and G band at 0.99 confirms that the laser-generated graphene structure has multiple defects. Furthermore, a broadened 2D band is observed in the region from 2700 to 3000 cm^{-1}. This is due to the second order process of double resonance Raman scattering resulting in two phonon emissions near the K point of the Brillouin zone and is strongly dependent on the phonon structure of graphene.
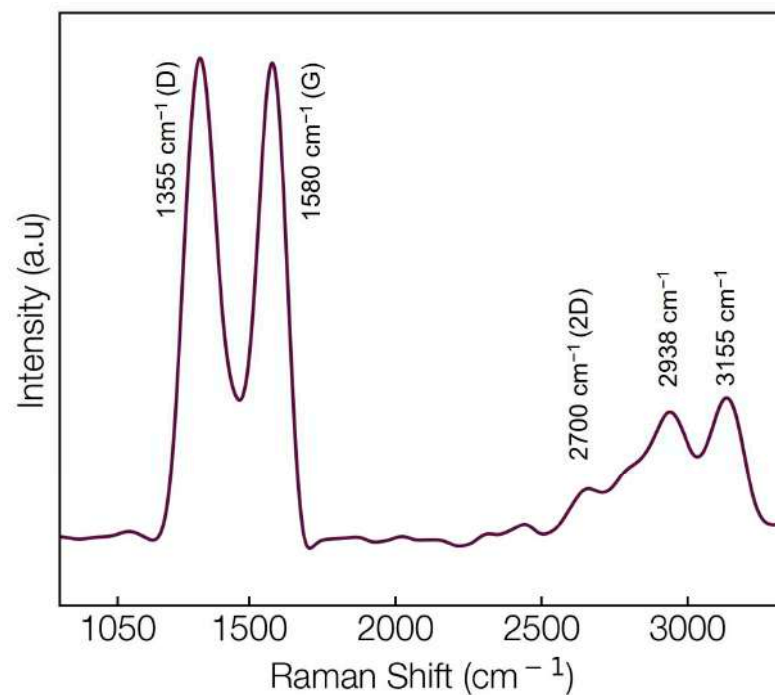

Figure 3. Raman spectra of generated LIG.

Consequently, unlike the presence of a monolayer graphene, which has a single Raman shift at 2700 cm^{-1}, the broadening in this study indicates the presence of a multi-layered structure. Additionally, the oxygen-based functional groups prevent efficient stacking of the graphene layers, causing a slight shift in the peak appearance [46]. Another interesting observation regards the Raman shift peak at ~2930 cm^{-1}. Few studies have attributed the peak due to the presence of C-H bonds. Also, the peak present at 3165 cm^{-1} is correlated to the presence of hydroxyl and carboxylic functional groups [47,48]. Herein, it is important to emphasize that the term laser-induced graphene (LIG) refers to the formation of a reduced graphene oxide (rGO)-based structure and not a monolayer 2D Graphene. However, with the piezoresistive sensing properties as a focus, rGO is an affordable alternative for strain sensing applications even on large scale applications [49,50].

3.2. Piezoresistive Properties

After the characterization of the material properties of the fabricated LIG, its piezo-resistivity was characterized for strain sensing applications. A standard three-point bending test as shown in Figure 4a was employed to investigate the ability of the LIG fabricated in this work to sense flexural strain along with continuous measurement of resistance change. From the test results, the gauge factor (GF) of the sensor was calculated using the following formula.

$$GF = (\Delta R/R)/\varepsilon \qquad (1)$$

where ΔR is the change in resistance, R is the zero-strain resistance, and ε is the applied strain during the bend test. Figure 4b shows the plot of normalized resistance change corresponding to applied strain.
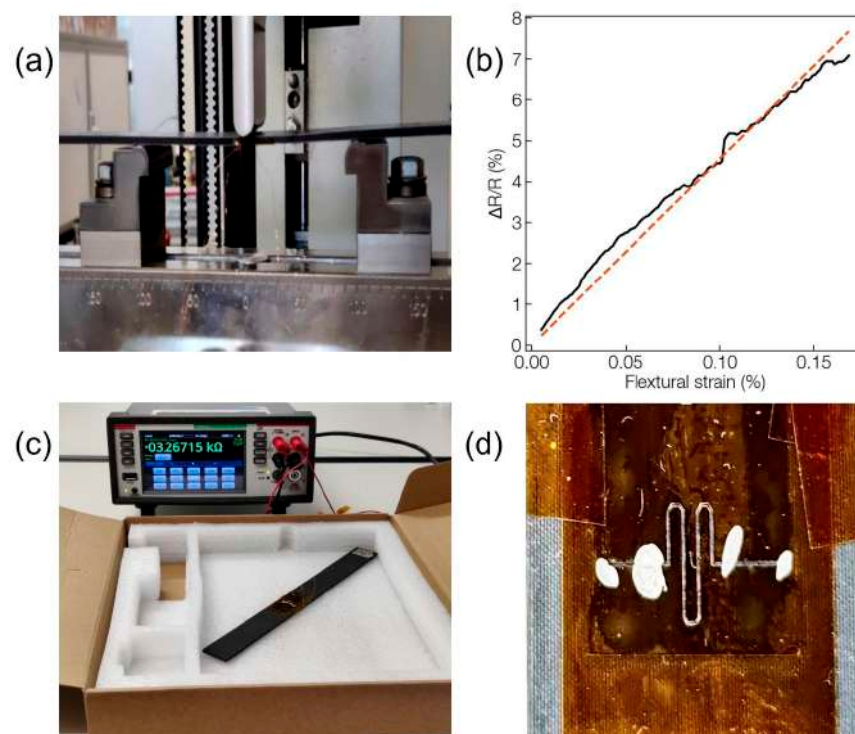
Figure 4. (**a**) Relative resistance change vs applied flexural strain, (**b**) Three-point bend test setup during measurement, (**c**) Strain-gauge connected to the multimeter, (**d**) Close view of the LIG sensor circuit.

The obtained data show a linear trend up to the measured strain of 0.16%, and a linear fit provided a GF of 40. It is worth mentioning that the commercial strain sensors typically display a GF < 5, which confirms the good sensitivity of the fabricated LIG sensor.

3.3. Superhydrophobic Property

In addition to the good strain sensing performance of the fabricated LIG, the laser parameter for the strain sensor was primarily selected to result in the ultrahydrophobic property of the fabricated LIG sensor, here termed SH-LIG. Figure 5a shows a 6 µL water droplet on the fabricated superhydrophobic surface. The droplet maintains a high contact angle (165°) and low roll-off (5°) from the surface, an indication of an extreme superhydrophobic surface. Additionally, as demonstrated in Figure 5b and the video in the supplementary information, the impinging water droplets are totally repelled from the surface as a result of minimal surface interaction, causing the water droplets to rebound and exit the surface. It is worth mentioning that the contact angle values obtained in the single-step laser processing in this study stand better than previous studies on superhydrophobic LIG fabrication with water contact angles closer to 155°.
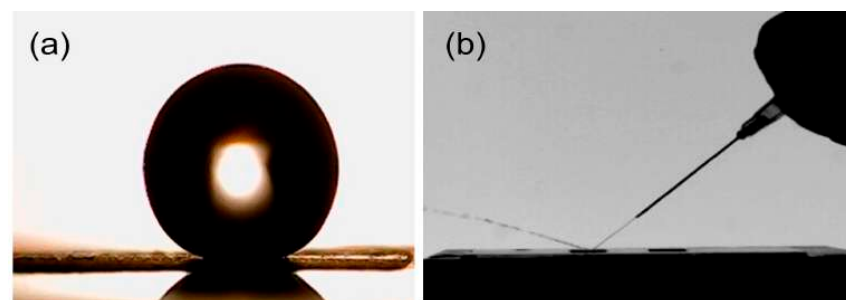

Figure 5. (**a**) 6 µL water droplet above SH-LIG surface on a glass substrate, (**b**) Water jet bouncing off the SH-LIG.

The laser ablation of the polyimide tape generates the LIG, which is directly deposited over the substrate itself. The unmodified polyimide tape can then be peeled off, rendering the pristine substrate with the specific laser patterned SH-LIG. The SH-LIG can be generated on different substrates as shown in Figure 6. Topographical surface analysis was performed over the SH-LIG on different substrates to determine the surface roughness, which is an important parameter to define superhydrophobic surfaces. Table 1 shows the measured average surface roughness (Sa) of the SH-LIG region over the substrates. Noticeably, the average surface roughness of SH-LIG modification varies drastically between the different substrates. This effect can be attributed to the difference in the material properties of the substrates. Although the average surface roughness varies noticeably, all the samples exhibited excellent superhydrophobic property with static contact angles above 160° and roll-off angles below 5° for all the samples.
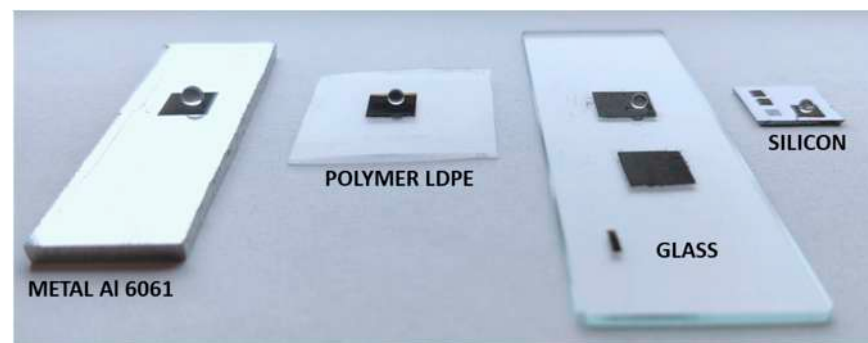

Figure 6. SH-LIG fabricated on different substrates in a one-step laser process.

Table 1. Profilometer analysis of average surface roughness of SH-LIG on various substrates.

Substrate	Roughness [Sa (μm)]
Al 6061	6.22
Silicon	1.81
Glass	4.58

Therefore, in terms of surface morphology, eventhough the microtexture varies on different samples, the excellent superhydrophobicity can be considered a result of the hierarchical micro/nano surface feature of LIG. The laser-modified micro-scale roughness along with the porous and fibrous nano-scale complex graphene oxide network provides an excellent surface feature to facilitate ultrahydrophobicity. Apart from the topographical analysis, the surface elemental compositional analysis was performed using energy dispersive X-ray spectroscopy. EDS analysis was performed on the glass, aluminum, and silicon substrates. Table 2 shows the quantitative information of the SH-LIG on different substrates. The corresponding EDS spectra are shown in Figure S1.

Table 2. EDS composition information of different SH-LIG substrates.

Element	Atomic %		
	Al 6061	Silicon	Glass
Al	40.5	-	-
Si	-	69.2	18.7
C	28.5	23.3	45.9
O	29.1	7.4	35.5

The EDS analysis confirms the presence of carbon as a major elemental component in all the samples. For all the samples, the pristine samples had a carbon content of below 8%. By nature, carbonaceous materials are hydrophobic. The hydrophobic surface chemistry in combination with a hierarchical surface texture renders the surface ultrahydrophobic. Further, to analyze the surface functional groups responsible for the superhydrophobic nature, FTIR spectroscopic analysis was performed. Therefore, the SH-LIG is substrate-independent as demonstrated in Figure 6.

Interestingly, the fabricated SH-LIG was substrate-independent. Figure 6 shows the water droplets with high contact angles on SH-LIG on various substrates. In all the cases, the contact angle was greater than 160° and the roll-off was below 5°. FTIR spectroscopy was performed on the fabricated samples to analyze the surface chemical composition of the SH-LIG surface and understand its origin. To compare the effect of laser parameters on the resulting chemical composition of the SH-LIG, another laser-processed sample that used high average laser power (16 W) was prepared. Figure 7 represents the FTIR spectrum of both the samples mentioned above.
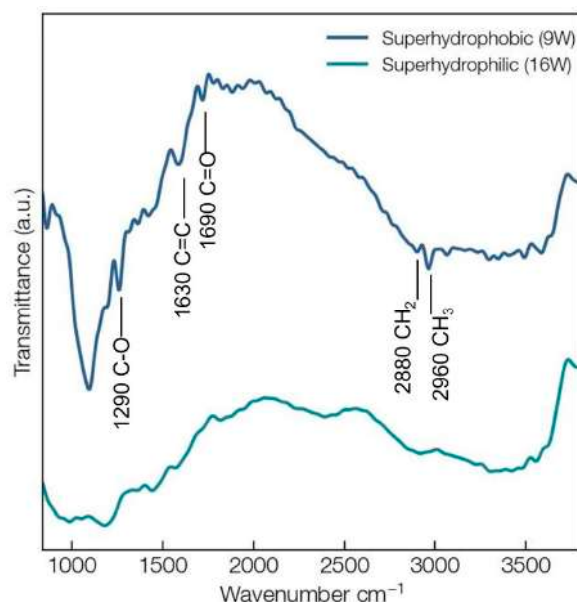

Figure 7. Comparison of FTIR spectra of superhydrophobic LIG and superhydrophilic laser modifications.

The FTIR spectrum collected from the SH-LIG shows an absorbance peak at 1290 cm^{-1} which is attributed to the presence of C-O bonds in alcohol or C-O-C functional group [51]. The absorption at ~1630 cm^{-1} corresponds to the C=C stretching in the aromatic rings [52]. Additionally, the absorption at 1690 cm^{-1} is associated with the typical C=O stretch of the carbonyl group [53]. Further, the absorption at ~2880 and 2960 cm^{-1} corresponds to the stretching of CH$_2$ and CH$_3$ groups, respectively [54]. In comparison, the FTIR spectra of the sample modified at high average power do not show the presence of any significant peak at corresponding wavenumbers. This could be a result of the strong photothermal effect at high temperatures leading to strong oxidation and thus superhydrophilicity of the fabricated LIG [55].

An important aspect of superhydrophobic surface functionality lies in the stability of the property, especially in extreme environments. Therefore, SH-LIG was fabricated on both glass and composite materials to test their stability during immersion under water for 25 h. In the case of the composite material, an identical line circuit pattern with silver paste contacts, similar to the one used in the three-point bend test, was prepared to test the resistance change with immersion time. However, an 8 mm × 8 mm area of SH-LIG was generated on a glass substrate to measure the variation in water contact angle with immersion time. As shown in Figure 8, the dynamic contact angle measurements demon-

strate the stability of the SH-LIG even after continuous immersion underwater for 25 h. An important aspect of the dynamic contact angle measurement is the contact angle hysteresis (CAH), which is the difference between advancing and receding contact angles. In this study, even after 25 h of immersion, the CAH is ~6.8°, thus maintaining a stable superhydrophobicity. This demonstrates the high stability of the superhydrophobic property, which is a combined effect of the hydrophobic carbonaceous LIG and the hierarchical and fibrous surface morphology efficiently trapping air and repelling water penetration [56–59].
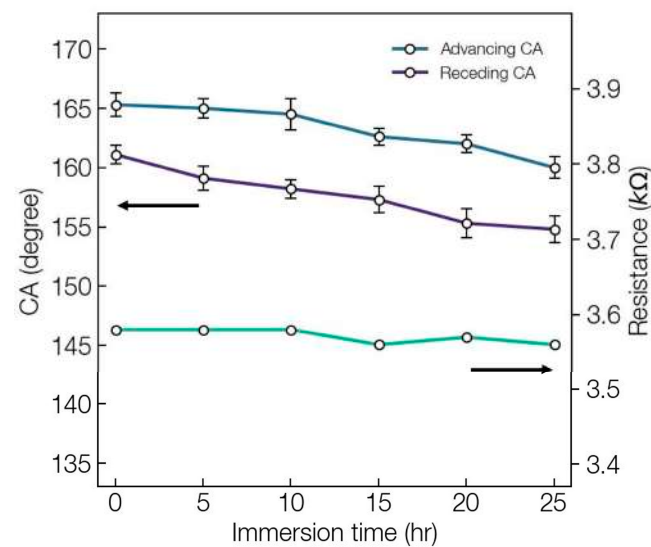

Figure 8. Dynamic contact angle measurements on the SH-LIG modified area and electrical resistance measurements performed on a SH-LIG conduction line circuit (green line) at different time intervals up to 25 h.

From Figure 8, the stability in superhydrophobicity is further confirmed by the circuit resistance measurements performed on a SH-LIG conduction line circuit of 2.5 cm length, at various time intervals on the LIG fabricated on the composite material which was immersed underwater. The resistance values remain almost the same after 25 h due to the stability of its superhydrophobic property.

Figure 9 shows the effect of total internal reflection by the trapped thin air layer, also termed plastron, on the SH-LIG, causing a shiny appearance of the superhydrophobic region on water immersion. On the other hand, the circuit resistance of the SH-LIG prepared on the composite material stays almost constant, with a negligible variation of less than 1%. This further confirms the remarkable stability of the fabricated SH-LIG under complete immersion conditions.
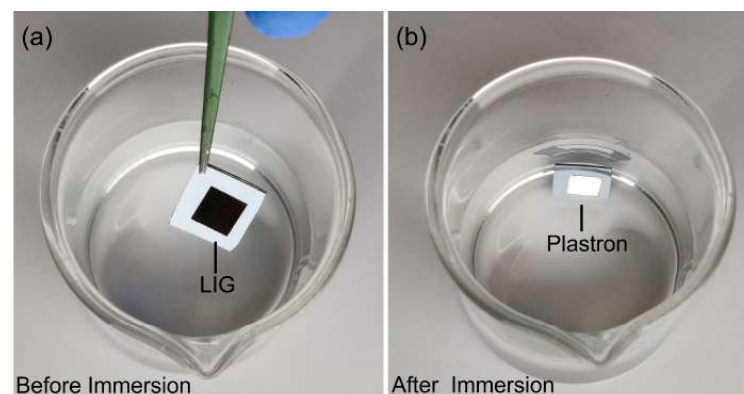

Figure 9. Depiction of highly reflective plastron (thin air film) layer over the superhydrophobic LIG on silicon surface (**a**) before immersion (**b**) after immersion.

High-speed camera images in Figure 10a,b, show the droplet bounce behavior before and after water immersion for 24 h. Indeed, the droplet bounce characteristics provide a direct means to examine the surface's ultrahydropohibc property due to the energy exchange involved on surface impact. The contact time of the droplet (6 µL) on the superhydrophobic surface from impact (1.0 m/s) to lift-off is considered as the analysis parameter in this study.
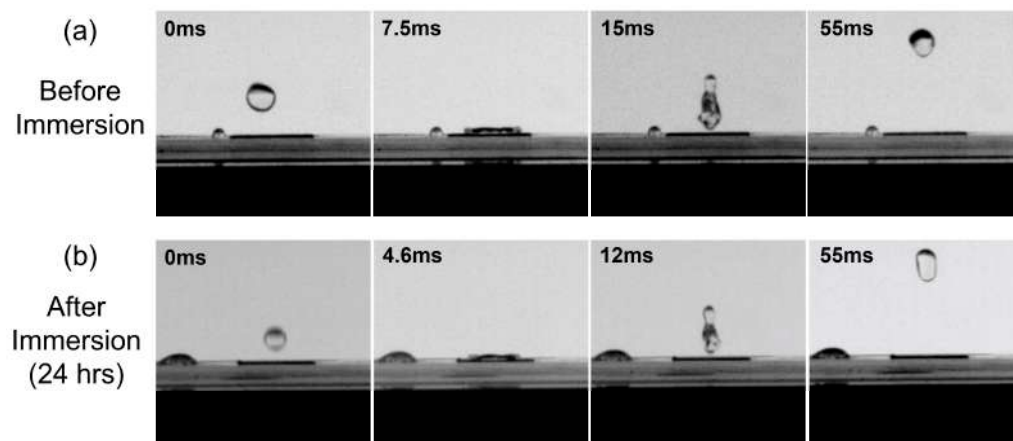

Figure 10. (**a**) Impact and bounce of water-droplet on the SH-LIG before immersion and (**b**) after immersion in de-ionized water for 24 h.

In coherence with the droplet bounce behavior on artificial ultrahydrophobic surfaces, the drop spreads like a thin sheet to a maximum diameter, recoils, and leaves the surface for both the tested surfaces [60,61]. For the freshly prepared SH-LIG, the droplet lifts off within 11.2 ms; for the immersed SH-LIG, the droplet lift-off occurs within 12.1 ms. The contact time is similar for both surfaces and relates to the droplet bounce behavior on conventional biomimetic ultrahydrophobic surfaces. Such surfaces with reduced contact time have the potential for pagophobic applications [62]. The SH-LIG surfaces fabricated in this study demonstrate stable water-repellence properties, bolstering the applicational prospects of substrate-independent laser-based graphene oxide devices.

4. Conclusions

In summary, a DLW approach was used to fabricate reduced graphene oxide from a polyimide-based precursor. The rGO on a CFRP composite performed as an excellent strain gauge with GF ~40, which is much higher than that of commercial strain gauges with GF below a value of 5. Further, the rGO could be prepared on various substrates ranging from metals to polymers and showed excellent superhydrophobic properties in all cases. The superhydrophobicity was also stable upon complete immersion under water for 25 h. In particular, a laser-based approach that combines flexibility with the substrate-independent one-step fabrication of stable superhydrophobicity extends the scope of LIG based sensors for even extreme environments.

References

1. Koumoulos, E.; Trompeta, A.-F.; Santos, R.-M.; Martins, M.; Santos, C.; Iglesias, V.; Böhm, R.; Gong, G.; Chiminelli, A.; Verpoest, I.; et al. Research and Development in Carbon Fibers and Advanced High-Performance Composites Supply Chain in Europe: A Roadmap for Challenges and the Industrial Uptake. *J. Compos. Sci.* **2019**, *3*, 86. [CrossRef]

2. Scattareggia Marchese, S.; Epasto, G.; Crupi, V.; Garbatov, Y. Tensile Response of Fibre-Reinforced Plastics Produced by Additive Manufacturing for Marine Applications. *JMSE* **2023**, *11*, 334. [CrossRef]

3. Zhang, C.; Ling, Y.; Zhang, X.; Liang, M.; Zou, H. Ultra-Thin Carbon Fiber Reinforced Carbon Nanotubes Modified Epoxy Composites with Superior Mechanical and Electrical Properties for the Aerospace Field. *Compos. Part A Appl. Sci. Manuf.* **2022**, *163*, 107197. [CrossRef]

4. Jani, S.P.; Sajith, S.; Rajaganapathy, C.; Adam Khan, M. Mechanical and Thermal Insulation Properties of Surface-Modified Agave Americana/Carbon Fibre Hybrid Reinforced Epoxy Composites. *Mater. Today Proc.* **2021**, *37*, 1648–1653. [CrossRef]

5. Bartkowiak, M.; Kizak, M.; Liebig, W.V.; Weidenmann, K.A. Fatigue Behavior of Hybrid Continuous-Discontinuous Fiber-Reinforced Sheet Molding Compound Composites under Application-Related Loading Conditions. *Compos. Part C Open Access* **2022**, *8*, 100265. [CrossRef]

6. Zheng, H.; Zhang, W.; Li, B.; Zhu, J.; Wang, C.; Song, G.; Wu, G.; Yang, X.; Huang, Y.; Ma, L. Recent Advances of Interphases in Carbon Fiber-Reinforced Polymer Composites: A Review. *Compos. Part B Eng.* **2022**, *233*, 109639. [CrossRef]

7. Barile, C.; Casavola, C.; Pappalettera, G.; Paramsamy Kannan, V. Damage Monitoring of Carbon Fibre Reinforced Polymer Composites Using Acoustic Emission Technique and Deep Learning. *Compos. Struct.* **2022**, *292*, 115629. [CrossRef]

8. Sun, Q.; Zhou, G.; Meng, Z.; Jain, M.; Su, X. An Integrated Computational Materials Engineering Framework to Analyze the Failure Behaviors of Carbon Fiber Reinforced Polymer Composites for Lightweight Vehicle Applications. *Compos. Sci. Technol.* **2021**, *202*, 108560. [CrossRef]

9. Forintos, N.; Sarkadi, T.; Czigany, T. Electric Resistance Measurement–Based Structural Health Monitoring with Multifunctional Carbon Fibers: Predicting, Sensing, and Measuring Overload. *Compos. Commun.* **2021**, *28*, 100913. [CrossRef]

10. Li, H.; Zhang, J.; Chen, J.; Luo, Z.; Zhang, J.; Alhandarish, Y.; Liu, Q.; Tang, W.; Wang, L. A Supersensitive, Multidimensional Flexible Strain Gauge Sensor Based on Ag/PDMS for Human Activities Monitoring. *Sci. Rep.* **2020**, *10*, 4639. [CrossRef]

11. Ahuja, P.; Akiyama, S.; Ujjain, S.K.; Kukobat, R.; Vallejos-Burgos, F.; Futamura, R.; Hayashi, T.; Kimura, M.; Tomanek, D.; Kaneko, K. A Water-Resilient Carbon Nanotube Based Strain Sensor for Monitoring Structural Integrity. *J. Mater. Chem. A* **2019**, *7*, 19996–20005. [CrossRef]

12. Sun, R.; Gao, L.; Liu, F.; Su, H.; Wu, L.; Zou, Z.; Wu, L.; Zhang, H.; Liao, C. Magnetically Induced Robust Anisotropic Structure of Multi-Walled Carbon Nanotubes/Ni for High-Performance Flexible Strain Sensor. *Carbon* **2022**, *194*, 185–196. [CrossRef]

13. Fu, Y.-F.; Li, Y.-Q.; Liu, Y.-F.; Huang, P.; Hu, N.; Fu, S.-Y. High-Performance Structural Flexible Strain Sensors Based on Graphene-Coated Glass Fabric/Silicone Composite. *ACS Appl. Mater. Interfaces* **2018**, *10*, 35503–35509. [CrossRef]

14. Qian, C.; Xiao, T.; Chen, Y.; Wang, N.; Li, B.; Gao, Y. 3D Printed Reduced Graphene Oxide/Elastomer Resin Composite with Structural Modulated Sensitivity for Flexible Strain Sensor. *Adv. Eng. Mater.* **2021**, *24*, 2101068. [CrossRef]

15. Lei, M.; Feng, K.; Ding, S.; Wang, M.; Dai, Z.; Liu, R.; Gao, Y.; Zhou, Y.; Xu, Q.; Zhou, B. Breathable and Waterproof Electronic Skin with Three-Dimensional Architecture for Pressure and Strain Sensing in Nonoverlapping Mode. *ACS Nano* **2022**, *16*, 12620–12634. [CrossRef]

16. Smeacetto, F.; Zanchi, E.; Menon, D.M.N.; Janner, D.; Lamnini, S.; Salvo, M.; De La Pierre, S.; Javed, H.; Ferraris, M. Torsional Behaviour of Glass-Joined, Laser-Processed Crofer 22 APU Interconnect: Unravelling the Effect of Surface Roughness on the Shear Strength. *Ceram. Int.* **2022**, *48*, 32837–32843. [CrossRef]

17. Menon, D.M.N.; Pugliese, D.; Janner, D. Infrared Nanosecond Laser Texturing of Cu-Doped Bioresorbable Calcium Phosphate Glasses. *Appl. Sci.* **2022**, *12*, 3516. [CrossRef]

18. Zhu, J.; Huang, X.; Song, W. Physical and Chemical Sensors on the Basis of Laser-Induced Graphene: Mechanisms, Applications, and Perspectives. *ACS Nano* **2021**, *15*, 18708–18741. [CrossRef]

19. Liu, K.; Yang, C.; Zhang, S.; Wang, Y.; Zou, R.; Alamusi; Deng, Q.; Hu, N. Laser Direct Writing of a Multifunctional Superhydrophobic Composite Strain Sensor with Excellent Corrosion Resistance and Anti-Icing/Deicing Performance. *Mater. Des.* **2022**, *218*, 110689. [CrossRef]

20. Guo, Y.; Zhang, C.; Chen, Y.; Nie, Z. Research Progress on the Preparation and Applications of Laser-Induced Graphene Technology. *Nanomaterials* **2022**, *12*, 2336. [CrossRef]

21. Wang, W.; Lu, L.; Li, Z.; Lin, L.; Liang, Z.; Lu, X.; Xie, Y. Fingerprint-Inspired Strain Sensor with Balanced Sensitivity and Strain Range Using Laser-Induced Graphene. *ACS Appl. Mater. Interfaces* **2022**, *14*, 1315–1325. [CrossRef]

22. Zhao, J.; Gui, J.; Luo, J.; Gao, J.; Zheng, C.; Xu, R. Highly Responsive Screen-Printed Asymmetric Pressure Sensor Based on Laser-Induced Graphene. *J. Micromech. Microeng.* **2022**, *32*, 015002. [CrossRef]

23. Li, Q.; Wu, T.; Zhao, W.; Ji, J.; Wang, G. Laser-Induced Corrugated Graphene Films for Integrated Multimodal Sensors. *ACS Appl. Mater. Interfaces* **2021**, *13*, 37433–37444. [CrossRef] [PubMed]

24. Hui, X.; Sharifuzzaman, M.; Sharma, S.; Park, C.I.; Yoon, S.; Kim, D.H.; Park, J.Y. A Nanocomposite-Decorated Laser-Induced Graphene-Based Multi-Functional Hybrid Sensor for Simultaneous Detection of Water Contaminants. *Anal. Chim. Acta* **2022**, *1209*, 339872. [CrossRef] [PubMed]

25. Li, B.; Luo, J.; Huang, X.; Lin, L.; Wang, L.; Hu, M.; Tang, L.; Xue, H.; Gao, J.; Mai, Y.-W. A Highly Stretchable, Super-Hydrophobic Strain Sensor Based on Polydopamine and Graphene Reinforced Nanofiber Composite for Human Motion Monitoring. *Compos. Part B Eng.* **2020**, *181*, 107580. [CrossRef]

26. Gao, W.-C.; Wu, W.; Chen, C.-Z.; Zhao, H.; Liu, Y.; Li, Q.; Huang, C.-X.; Hu, G.; Wang, S.-F.; Shi, D.; et al. Design of a Superhydrophobic Strain Sensor with a Multilayer Structure for Human Motion Monitoring. *ACS Appl. Mater. Interfaces* **2022**, *14*, 1874–1884. [CrossRef] [PubMed]

27. Wang, L.; Li, J.; Chen, Z.; Song, Z.; Meng, X.; Chen, X. Porous Graphene-Based Photothermal Superhydrophobic Surface for Robust Anti-Icing and Efficient De-Icing. *Adv. Mater. Interfaces* **2022**, *9*, 2201758. [CrossRef]

28. Li, Y.; Luong, D.X.; Zhang, J.; Tarkunde, Y.R.; Kittrell, C.; Sargunaraj, F.; Ji, Y.; Arnusch, C.J.; Tour, J.M. Laser-Induced Graphene in Controlled Atmospheres: From Superhydrophilic to Superhydrophobic Surfaces. *Adv. Mater.* **2017**, *29*, 1700496. [CrossRef]

29. Lee, Y.A.; Lim, J.; Cho, Y.; Lee, H.; Park, S.; Lee, G.-W.; Yoo, C.-Y.; Park, S.H.; Matham Murukeshan, V.; Kim, S.; et al. Attachable Micropseudocapacitors Using Highly Swollen Laser-Induced-Graphene Electrodes. *Chem. Eng. J.* **2020**, *386*, 123972. [CrossRef]

30. Liu, F.; Wang, G.; Ding, X.; Luo, S. Multifunctional Laser-Induced Graphene Enabled Polymeric Composites. *Compos. Commun.* **2021**, *25*, 100714. [CrossRef]

31. Wang, W.; Lu, L.; Li, Z.; Xie, Y. Laser Induced 3D Porous Graphene Dots: Bottom-up Growth Mechanism, Multi-Physics Coupling Effect and Surface Wettability. *Appl. Surf. Sci.* **2022**, *592*, 153242. [CrossRef]

32. Wakabayashi, S.; Arie, T.; Akita, S.; Nakajima, K.; Takei, K. A Multitasking Flexible Sensor via Reservoir Computing. *Adv. Mater.* **2022**, *34*, 2201663. [CrossRef]

33. Wang, L.; Wang, Z.; Bakhtiyari, A.N.; Zheng, H. A Comparative Study of Laser-Induced Graphene by CO_2 Infrared Laser and 355 Nm Ultraviolet (UV) Laser. *Micromachines* **2020**, *11*, 1094. [CrossRef] [PubMed]

34. Stanford, M.G.; Yang, K.; Chyan, Y.; Kittrell, C.; Tour, J.M. Laser-Induced Graphene for Flexible and Embeddable Gas Sensors. *ACS Nano* **2019**, *13*, 3474–3482. [CrossRef]

35. Gupta, A.; Sharma, C.P.; Thamaraiselvan, C.; Pisharody, L.; Powell, C.D.; Arnusch, C.J. Low-Voltage Bacterial and Viral Killing Using Laser-Induced Graphene-Coated Non-Woven Air Filters. *ACS Appl. Mater. Interfaces* **2021**, *13*, 59373–59380. [CrossRef] [PubMed]

36. Chen, Y.; Xie, B.; Long, J.; Kuang, Y.; Chen, X.; Hou, M.; Gao, J.; Zhou, S.; Fan, B.; He, Y.; et al. Interfacial Laser-Induced Graphene Enabling High-Performance Liquid−Solid Triboelectric Nanogenerator. *Adv. Mater.* **2021**, *33*, 2104290. [CrossRef]

37. Du, Q.; Chen, T.; Liu, J.; Zeng, X. Surface Microstructure and Chemistry of Polyimide by Single Pulse Ablation of Picosecond Laser. *Appl. Surf. Sci.* **2018**, *434*, 588–595. [CrossRef]

38. Bounos, G.; Selimis, A.; Georgiou, S.; Rebollar, E.; Castillejo, M.; Bityurin, N. Dependence of Ultraviolet Nanosecond Laser Polymer Ablation on Polymer Molecular Weight: Poly (Methyl Methacrylate) at 248 Nm. *J. Appl. Phys.* **2006**, *100*, 114323. [CrossRef]

39. Ma, W.; Zhu, J.; Wang, Z.; Song, W.; Cao, G. Recent Advances in Preparation and Application of Laser-Induced Graphene in Energy Storage Devices. *Mater. Today Energy* **2020**, *18*, 100569. [CrossRef]

40. Peng, Z.; Lin, J.; Ye, R.; Samuel, E.L.G.; Tour, J.M. Flexible and Stackable Laser-Induced Graphene Supercapacitors. *ACS Appl. Mater. Interfaces* **2015**, *7*, 3414–3419. [CrossRef]

41. Malyshev, A.Y.; Bityurin, N.M. Laser Swelling Model for Polymers Irradiated by Nanosecond Pulses. *Quantum Electron.* **2005**, *35*, 825–830. [CrossRef]

42. Marla, D.; Zhang, Y.; Hattel, J.H.; Spangenberg, J. Modeling of Nanosecond Pulsed Laser Processing of Polymers in Air and Water. *Model. Simul. Mater. Sci. Eng.* **2018**, *26*, 055005. [CrossRef]

43. Han, C.; Zahid, M.A.; Lee, B.; Oh, J.-Y.; Kim, Y.; Yi, J. Ultraviolet Nanosecond Laser Ablation of Polyimide with Thermal and Nonthermal Effects near Threshold Fluence. *J. Laser Appl.* **2022**, *34*, 032004. [CrossRef]

44. Bityurin, N. 8 Studies on Laser Ablation of Polymers. *Annu. Rep. Prog. Chem. Sect. C* **2005**, *101*, 216. [CrossRef]

45. Cardoso, A.R.; Marques, A.C.; Santos, L.; Carvalho, A.F.; Costa, F.M.; Martins, R.; Sales, M.G.F.; Fortunato, E. Molecularly-Imprinted Chloramphenicol Sensor with Laser-Induced Graphene Electrodes. *Biosens. Bioelectron.* **2019**, *124–125*, 167–175. [CrossRef]

46. Wahab, H.; Jain, V.; Tyrrell, A.S.; Seas, M.A.; Kotthoff, L.; Johnson, P.A. Machine-Learning-Assisted Fabrication: Bayesian Optimization of Laser-Induced Graphene Patterning Using in-Situ Raman Analysis. *Carbon* **2020**, *167*, 609–619. [CrossRef]

47. Sehat, A.A.; Khodadadi, A.A.; Shemirani, F.; Mortazavi, Y. Fast Immobilization of Glucose Oxidase on Graphene Oxide for Highly Sensitive Glucose Biosensor Fabrication. *Int. J. Electrochem. Sci.* **2015**, *10*, 272–286.

48. Hazra, K.S.; Rafiee, J.; Rafiee, M.A.; Mathur, A.; Roy, S.S.; McLauhglin, J.; Koratkar, N.; Misra, D.S. Thinning of Multilayer Graphene to Monolayer Graphene in a Plasma Environment. *Nanotechnology* **2011**, *22*, 025704. [CrossRef]

49. Nag, A.; Alahi, M.E.E.; Mukhopadhyay, S.C. Recent Progress in the Fabrication of Graphene Fibers and Their Composites for Applications of Monitoring Human Activities. *Appl. Mater. Today* **2021**, *22*, 100953. [CrossRef]

50. Ebrahimi, G.; Pakchin, P.S.; Shamloo, A.; Mota, A.; de la Guardia, M.; Omidian, H.; Omidi, Y. Label-Free Electrochemical Microfluidic Biosensors: Futuristic Point-of-Care Analytical Devices for Monitoring Diseases. *Microchim. Acta* **2022**, *189*, 252. [CrossRef]

51. Zelenková, G.; Zelenka, T.; Almáši, M.; Soldánová, M. Graphene as a Promising Additive to Hierarchically Porous Carbon Monoliths for Enhanced H_2 and CO_2 Sorption. *J. CO2 Util.* **2023**, *68*, 102371. [CrossRef]

52. Selim, M.S.; Fatthallah, N.A.; Higazy, S.A.; Chen, X.; Hao, Z. Novel Blade-like Structure of Reduced Graphene Oxide/α-Mn_2O_3 Nanocomposite as an Antimicrobial Active Agent against Aerobic and Anaerobic Bacteria. *Mater. Chem. Phys.* **2023**, *298*, 127436. [CrossRef]

53. Barahuie, F.; Saifullah, B.; Dorniani, D.; Fakurazi, S.; Karthivashan, G.; Hussein, M.Z.; Elfghi, F.M. Graphene Oxide as a Nanocarrier for Controlled Release and Targeted Delivery of an Anticancer Active Agent, Chlorogenic Acid. *Mater. Sci. Eng. C* **2017**, *74*, 177–185. [CrossRef]

54. Gao, X.; Yokota, N.; Oda, H.; Tanaka, S.; Hokamoto, K.; Chen, P.; Xu, M. Preparation of Few-Layer Graphene by Pulsed Discharge in Graphite Micro-Flake Suspension. *Crystals* **2019**, *9*, 150. [CrossRef]

55. Ye, R.; James, D.K.; Tour, J.M. Laser-Induced Graphene. *Acc. Chem. Res.* **2018**, *51*, 1609–1620. [CrossRef] [PubMed]

56. Zhang, Y.; Wang, T.; Wu, M.; Wei, W. Durable Superhydrophobic Surface with Hierarchical Microstructures for Efficient Water Collection. *Surf. Coat. Technol.* **2021**, *419*, 127279. [CrossRef]

57. Ivvala, J.; Arora, H.S.; Grewal, H.S. Towards Development of Sustainable Metallic Superhydrophobic Materials. *Colloids Surf. A Physicochem. Eng. Asp.* **2023**, *663*, 131047. [CrossRef]

58. Menon, D.M.N.; Giardino, M.; Janner, D. Tunable Pulsewidth Nanosecond Laser Texturing: From Environment Friendly Superhydrophobic to Superamphiphobic Surfaces. *Appl. Surf. Sci.* **2023**, *610*, 155356. [CrossRef]

59. Sharifikolouei, E.; Najmi, Z.; Cochis, A.; Scalia, A.C.; Aliabadi, M.; Perero, S.; Rimondini, L. Generation of Cytocompatible Superhydrophobic Zr–Cu–Ag Metallic Glass Coatings with Antifouling Properties for Medical Textiles. *Mater. Today Bio.* **2021**, *12*, 100148. [CrossRef]

60. Liu, Y.; Moevius, L.; Xu, X.; Qian, T.; Yeomans, J.M.; Wang, Z. Pancake Bouncing on Superhydrophobic Surfaces. *Nat. Phys.* **2014**, *10*, 515–519. [CrossRef]

61. Li, H.; Zhang, K. Dynamic Behavior of Water Droplets Impacting on the Superhydrophobic Surface: Both Experimental Study and Molecular Dynamics Simulation Study. *Appl. Surf. Sci.* **2019**, *498*, 143793. [CrossRef]

62. Elzaabalawy, A.; Meguid, S.A. Development of Novel Icephobic Surfaces Using Siloxane-Modified Epoxy Nanocomposites. *Chem. Eng. J.* **2022**, *433*, 133637. [CrossRef]